Journal of Structural Geology, Vol. 11, No. 3, pp. 329 to 342, 1989
Printed in Great Britain

0191-8141/89 $03.00 + 0.00
Pergamon Press plc

Sliding behavior and deformation textures of heated illite gouge

D. E. MOORE, R. SUMMERS and J. D. BYERLEE

U.S. Geological Survey, Menlo Park, CA 94025, U.S.A.

(*Received* 5 *March* 1987; *accepted in revised form* 10 *September* 1988)

Abstract—The run products of a series of triaxial friction experiments on an illite-rich gouge have been examined petrographically to study the relationship between textural development and sliding mode. The samples show a complete range of textures, from ones in which the entire gouge layer is deformed to ones in which the deformation is concentrated along narrow subsidiary shears and the rest of the gouge layer is massive. The samples with a pervasively developed deformation fabric slide stably, whereas the samples containing shear bands show stick–slip motion if the intersection angles between boundary–parallel and cross-cutting (Riedel) shears are also relatively high. These textural differences suggest that localization of shear combined with higher-angle Riedel shears are somehow involved in stick–slip motion. The orientation of Riedel-type shears in natural fault zones may also have potential as a paleoseismological tool.

INTRODUCTION

THIS paper describes the results of a petrographic study of the deformation textures developed during triaxial friction experiments on heated fault gouge. Preliminary textural studies on a group of four gouges tested at two sliding velocities had revealed some possible correlations between gouge texture and velocity (Moore *et al.* 1986a). The four gouges examined were montmorillonite- and serpentine-rich gouges from the San Andreas fault zone, a crushed granite and an illite-rich gouge. At the slower velocity, the gouges showed less of a mineral fabric, fewer stretched grains, and higher angles of intersection between fractures and shears that cross-cut the gouge layer and ones developed along the boundaries between the gouge and the enclosing rock cylinder. These same gouges also showed a greater tendency to stick–slip motion at the slower velocity; therefore, the deformation textures were of potential use in understanding the sliding behavior of the laboratory samples. Because the fracture and shearing patterns that develop during shear box, Riedel and triaxial friction tests have been generally correlated with natural fault zone traces (e.g. Tchalenko 1970, Wallace 1973, Rutter *et al.* 1986), any differences that can be found between the stably sliding and stick–slip experimental samples may also help to explain natural earthquake processes.

As a result of this preliminary work and its potential significance, we decided to expand our petrographic studies. The same illite-rich gouge that was described in Moore *et al.* (1986a) was being used in another set of friction experiments in our laboratory, so that a large number of samples of this gouge was available for study. We therefore decided to concentrate our efforts on the illite gouge, and we conducted additional experiments with it to provide samples under a variety of temperature, confining pressure, fluid pressure, and velocity conditions. In all, 93 run products of the illite gouge have been examined, which include many examples each of stable and stick–slip motion and a wide range of strengths. The results of this petrographic study, which form the basis of this paper, confirm the hypothesis of a correlation between the sliding behavior of the gouge and its deformation texture.

EXPERIMENTAL PROCEDURE

The apparatus used for the triaxial friction experiments at elevated temperatures is illustrated in Fig. 1. A layer of the illite gouge about 0.65 mm in initial thickness was placed along a finely ground 30° sawcut surface in a Westerly granite cylinder 19.0 mm in diameter and 41.3 mm long. The gouge-filled cylinder was placed within an annealed copper jacket between titanium carbide end

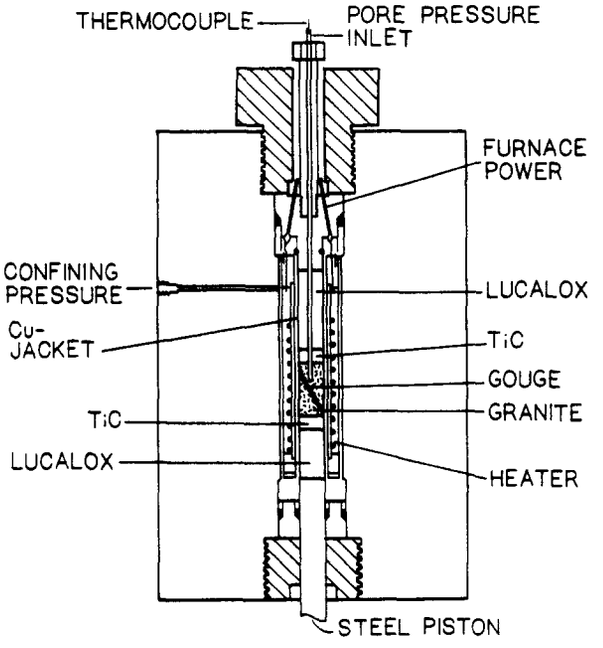

Fig. 1. Experimental sample assembly for triaxial friction experiments at elevated temperatures. In this diagram, the gouge-filled sawcut plane is oriented perpendicular to the plane of the page; all of the thin sections listed in Table 1 were cut to show this same orientation.

Table 1. Summary of experimental conditions and results

Expt No.	T (°C)	Velocity ($\mu m\,s^{-1}$)	P_p (MPa)	P_c (MPa)	Textural classification*	Riedel shear angles (°)	Sliding behavior
Experiments conducted for this study							
1411	200	4.8	0.1	50	c	8–11	Stable
1291	200	4.8	0.1	100	b	7–10	Stable
1412	200	4.8	0.1	140	b	5–7	Stable
1367	200	4.8	0.1	175	a	—	Stable
1413	200	4.8	0.1	210	b	3–7	Stable
1294	200	4.8	0.1	250	a	—	Stable
1416	400	4.8	0.1	25	c	7–12	Stick–slip (5 MPa)
1414	400	4.8	0.1	50	c	3–11	Stick–slip (11 MPa)
1363	400	4.8	0.1	100	c	6–14	Stick–slip (28 MPa)
1374	400	4.8	0.1	175	c	6–11	Stick–slip (22 MPa)
1297	400	4.8	0.1	250	c	2–10	Stick–slip (11 MPa)
1415	600	4.8	0.1	50	c	2–15	Stick–slip (36 MPa)
1293	600	4.8	0.1	100	b	9–14	Stick–slip (54 MPa) to 3 mm; then stable
1369	600	4.8	0.1	175	c	7–17	Stick–slip (43 MPa)
1419	600	4.8	0.1	210	d	12–23	Stick–slip (480 MPa)
1296	600	4.8	0.1	250	b	8–14	Stable
1364	400	0.048	0.1	100	c	10–15	Stick–slip (50 MPa)
1365	600	0.048	0.1	100	d	13–21	Stick–slip (30–86 MPa)
Experiments from pore pressure/permeability study (Moore *et al.* 1986b)							
1315	200	4.8	10	110	a	—	Stable
1314	200	4.8	20	120	b	6	Stable
1313	200	4.8	30	130	b	4–6	Stable
1379	200	4.8	40	140	b	3–5	Stable
1312	200	4.8	50	150	b	0–9	Stable
1376	200	4.8	60	160	b	6–8	Stable
1311	200	4.8	70	170	b	2–8	Stable
1377	200	4.8	80	180	c	6–10	Stable
1316	200	4.8	90	190	a	—	Stable
1281	200	0.048	10	110	c	6–7	Stable
1282	200	0.048	15	115	d	2–8	Stable
1283	200	0.048	20	120	d	6–7	Stable
1329	200	0.048	30	130	c	3–14	Stable
1331	200	0.048	40	140	c	10–12	Stable
1328	200	0.048	50	150	d	6–9	Stable; a few irregularities
1335	200	0.048	60	160	d	0–9	Stable
1327	200	0.048	70	170	c	8–10	Stable
1334	200	0.048	80	180	c	6–8	Stable
1319	200	0.048	90	190	d	9	Stable
1299	400	4.8	20	120	c	0–15	Stick–slip (32 MPa)
1300	400	4.8	30	130	c	7–18	Stick–slip (43 MPa)
1361	400	4.8	40	140	c	9–13	Stick–slip (18 MPa)
1301	400	4.8	50	150	d	10–12	Stick–slip (25 MPa)
1360	400	4.8	60	160	c	9–14	Stick–slip (29 MPa)
1302	400	4.8	70	170	c	0–13	Stick–slip (14 MPa)
1359	400	4.8	80	180	c	8–15	Stick-slip (11 MPa)
1303	400	4.8	90	190	c	14	Stick–slip (14 MPa)
1358	400	4.8	100	200	c	9–16?	Stick–slip (7 MPa)
1280	400	0.048	10	110	c	7–10	Stick–slip (70 MPa)
1279	400	0.048	15	115	c	3–11	Stick–slip (68 MPa)
1278	400	0.048	20	120	c	17	Stick–slip (80 MPa)
1277	400	0.048	25	125	c	0–16	Stick–slip (70 MPa)
1276	400	0.048	30	130	d	10–13	Stick–slip (43 MPa); short run
1349	400	0.048	40	140	b	13	Stable to 2 mm axial compression; then stick–slip (60 MPa)
1284	400	0.048	50	150	c	14–17	Stick–slip (50 MPa)
1348	400	0.048	60	160	c	8–14	Occasional stress drops (25 MPa)
1285	400	0.048	70	170	b	7	Mostly stable; T fluctuations?
1347	400	0.048	80	180	c	7–14	Stable to 2 mm; then stick–slip (68 MPa)
1287	400	0.048	90	190	c	4–6	Irregular; T fluctuations?
1346	400	0.048	100	200	c	5–14	Occasional stress drops ($\leq$ 165 MPa)
1317	600	4.8	10	110	b	9–13	Stick–slip (50 MPa) to 1.5 mm; then mostly stable
1308	600	4.8	20	120	b	10–11	Stick–slip (50 MPa) to 1.2 mm; then stable
1307	600	4.8	30	130	b	11	Stable
1326	600	4.8	40	140	b	7–12	Stick–slip (36 MPa) to 1 mm; then stable

Table 1. *Continued*

Expt No.	T (°C)	Velocity ($\mu m\ s^{-1}$)	P_p (MPa)	P_c (MPa)	Textural classification*	Riedel shear angles (°)	Sliding behavior
1306	600	4.8	50	150	b	10–13	Initially irregular; then stable
1325	600	4.8	60	160	b	5–12	Stick–slip (21–32 MPa) to 1 mm; then stable
1310	600	4.8	70	170	c	6–12	Stick–slip (21 MPa) to 1 mm; then stable
1324	600	4.8	80	180	b	5	Stable
1304	600	4.8	90	190	b	12	Stick–slip (18–29 MPa) to 1mm; then stable
1323	600	4.8	100	200	c	7–9	Stable
1267	600	0.048	10	110	d	6–19	Stick–slip (380 MPa)
1270	600	0.048	15	150	b	10–13	One 380 MPa stress drop; then stable
1269	600	0.048	20	120	d	21–22	Stick–slip (380 MPa)
1264	600	0.048	25	125	c	10	Stick–slip (75 MPa) to 1.3 mm; then irregular
1263	600	0.048	30	130	c	5–10	Irregular
1322	600	0.048	40	140	c	12–23	Stick–slip (65 MPa); max. strength at 1mm
1290	600	0.048	50	150	d	12–23	Stick–slip (70–200 MPa)
1321	600	0.048	60	160	c	7–8	Stable; T fluctuations
1289	600	0.048	70	170	c	16	Initially occasional stress drops; then stick–slip (75 MPa)
1320	600	0.048	80	180	c	6–8	Stable; T fluctuations
1318	600	0.048	90	190	c	10	Stable; T fluctuations
1262	600	0.048	100	200	c	3–14	Occasional stress drops ($\leq$ 22 MPa)
Illite thin sections from Moore *et al.* (1986a)							
1212	200	0.048	3	250	c	12	Stable
1151	400	4.8	3	100	c	Poor section	Stick–slip (25 MPa)
1157	400	4.8	3	250	b	2–11	Stick–slip (18 MPa) to 2mm; then stable
1150	600	4.8	3	100	d	9–24	Stick–slip (375–420 MPa)
1159	600	4.8	3	250	b	5–14	Stable
1261	600	0.048	3	100	d	15–27	Stick–slip (400–440 MPa)
1343	600	0.048	3	250	c	4–14	Stick–slip ($\leq$71 MPa) to 2.5 mm; then stable

*Based on diagrams (a)–(d) in Figs. 8 and 9.

pieces and Lucalox insulators. The jacketed assembly was placed in a cylindrically shaped resistance heater, and the space between the sample and the heater was loosely packed with boron nitride, which is a poor electrical and a good thermal conductor.

Confining and pore pressures were applied first to the jacketed sample. The pore fluids were introduced to the sample by means of a hole drilled partway through the upper granite cylinder (Fig. 1). Both granite pieces were presaturated with deionized water, to reduce the time required to stabilize the pore fluid in the sample. After these pressures had stabilized, the temperature was raised to the desired value. The sample was then held at temperature and pressure for 1800 s before the load was applied. Temperatures were monitored by a thermocouple inserted along the pore pressure inlet. Pressures and strains were computer-controlled and recorded; force and displacement measurements were made outside the pressure vessel using a load cell and displacement transducer. The confining and pore pressures were measured along the inlet lines outside the sample assembly.

The experimental conditions for each sample studied are summarized in Table 1. Each experiment was run at a temperature of 200, 400 or 600°C and at a strain rate of either 10^{-4} or $10^{-6}\ s^{-1}$, which corresponds to average sliding velocities (load point velocities) along the sawcut of 4.8 and $4.8 \times 10^{-2}\ \mu m\ s^{-1}$, respectively. These velocities refer to the average rate at which one granite piece slides past the other along the sawcut. For samples that show stick–slip motion, velocities within the gouge layer will differ significantly between the stick and the slip portions of each cycle. The pore fluid was deionized water; saline fluids more typical of natural groundwaters could not be used because they would have corroded the pore pressure system. Fluid chemistry should not, however, significantly affect the general textural features described in this study.

A group of experiments conducted specifically for this study was run at 0.1 MPa fluid pressure and confining pressures between 25 and 250 MPa. The illite samples examined by Moore *et al.* (1986a) from experiments at 3 MPa fluid pressure and 100 and 250 MPa confining pressure have also been included in this study. The rest of the experiments were run at higher pore pressures in the range of 10–100 MPa, and the confining pressures

were varied such that the effective pressure at room temperature was kept constant at 100 MPa. This latter group of experiments was conducted as part of a study of the effects of rapid heating on pore pressure and permeability of clay-bearing gouge. The purpose of that study was to simulate the effects that frictional heating accompanying an earthquake or premonitory slip can have on fault zone properties. Based on the results of those experiments, it should be emphasized that the values of pore pressure listed in Table 1 are the externally applied values.

Thin sections of the run products of the experiments were prepared for standard petrographic analysis. Most of the sections (86) were cut parallel to the long axis of the cylindrical sample and perpendicular to the plane of the sawcut. These sections show the length and thickness dimensions of the gouge layers, and they provide a view of gouge textures relative to the shear direction. Figure 7 is a low-power photomicrograph of one of these samples, showing the general appearance of the gouge layer and the surrounding granite sawcut pieces. The orientation here is the same as that in the friction apparatus (Fig. 1). Seven additional sections were cut across the cylinder axis but still perpendicular to the plane of the sawcut, to show the third or width dimension of the gouge samples. All of these latter thin sections were prepared from duplicate run products, and they are not included in Table 1 because the measurements of angles contained in the table could not be made on these samples.

RESULTS

Frictional strength and sliding behavior

Because of the large number of runs, only selected strength plots representative of the trends in strength and sliding mode with changing experimental conditions are presented in this paper (Figs. 2–5) (see Moore *et al.* 1986b, for most of the remaining strength plots). The sliding behavior of each individual sample is summarized in Table 1, however, for comparison with the deformation textures. At a given temperature and a low imposed pore pressure, increases in confining pressure lead to increases in the strength of the illite gouge; this effect is illustrated in Fig. 2, which plots samples at 200°C and 0.1 MPa pore pressure. Increasing the temperature under otherwise identical experimental conditions (e.g. Fig. 3) also produces an increase in the strength of the gouge as well as an increase in the tendency to stick–slip motion.

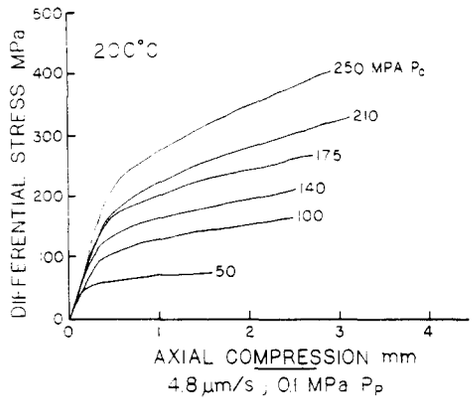

Fig. 2. Plot of differential stress against axial compression for illite gouge at 200°C and 0.1 MPa pore pressure, tested at different confining pressures.

Moving from low to high pore pressures at a constant imposed effective pressure (Figs. 3–5), no change in the strength of the gouge is discernible at 200°C, which is consistent with the effective stress law; at 400 and 600°C, however, the strength gradually decreases and the sliding behavior becomes progressively more stable. In the 400 and 600°C experiments at the faster velocity, some decrease in strength is apparent at pore pressures as low as 10 MPa, whereas at the slower velocity, the strength is unchanged at pore pressure below about 30 MPa (Moore

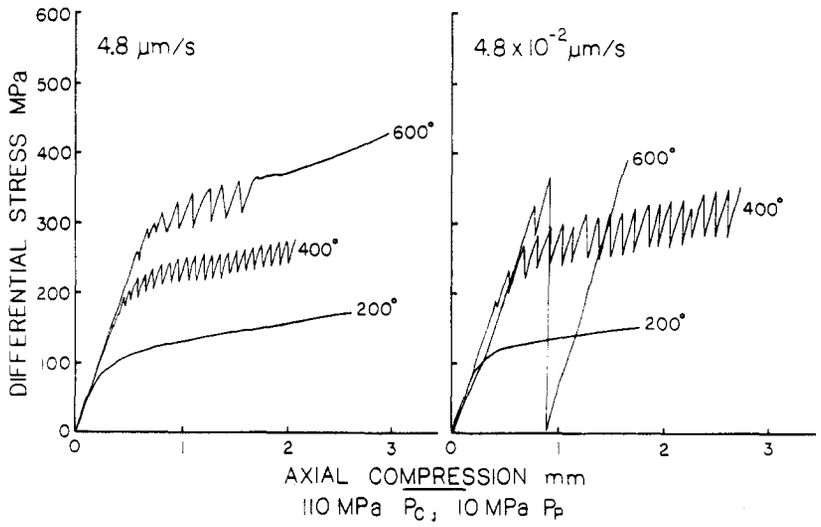

Fig. 3. Changes in frictional strength of illite gouge with increasing temperature for experiments at 10 MPa (room temperature) pore pressure and 110 MPa confining pressure. (Samples were heated and then held at temperature of test for 1800 s before the axial load was applied.)

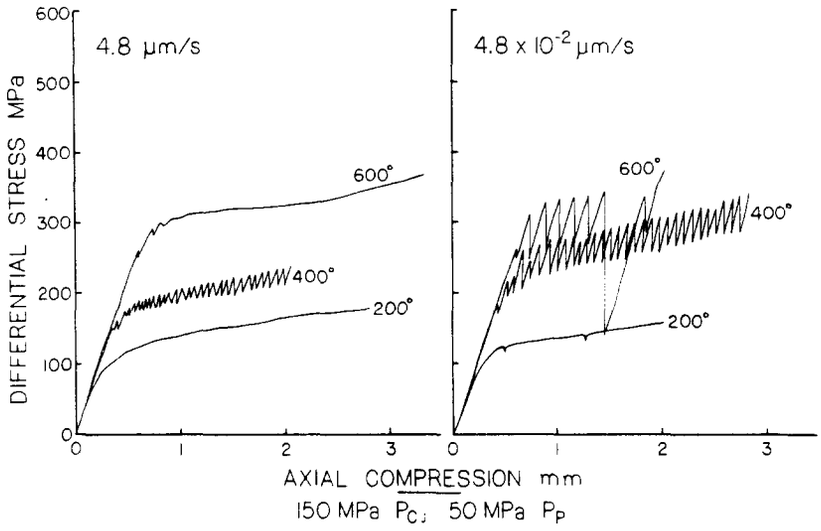

Fig. 4. Effect of increasing temperature on frictional strength of illite gouge, at 50 MPa (room temperature) pore pressure and 150 MPa confining pressure. (Samples were preheated for 1800 s before the axial load was applied.)

et al. 1986b). The observed reductions in strength in the experiments at high temperatures and pore pressures are probably the result of overpressurization of the fluids in the samples accompanying heating. The amount of pressure increase will be a function of the temperature change and the initial pore pressure, whereas the rate of alleviation of the excess pressure will be controlled by the permeability of the gouge. The illite gouge becomes noticeably compacted and lithified at high temperatures (Moore *et al.* 1983), and our hypothesis is that the lack of fluid-pressure equilibration in the samples is due to the lithified gouge having a very low permeability. This hypothesis will be tested by conducting high-temperature permeability measurements of the illite gouge, for calculation of fluid pressures in the samples and comparison with the observed strength reductions. The fact that the actual effective pressure within the gouge layer is unknown for this group of samples will not affect the comparison of gouge textures and sliding behavior. It should be noted, however, that any correlations described between textures and experimental conditions in this paper are limited to the experiments run at 0.1 and 3 MPa pore pressure.

Essentially all the 400 and 600°C samples show stick–slip motion at one or both of the load point velocities (Table 1). The steady-state coefficient of friction at constant velocity (μ_{ss}), which is an important parameter used by modelers, cannot be obtained from those data, because the velocity is continually changing from essentially stationary contact to an unknown velocity during sudden slip. The two 600°C samples in Fig. 5 show final periods of stable motion from which μ_{ss} could be measured. These two experiments may not be directly comparable, however, because of the probable lack of pore pressure equilibration. The effective pressure in the slower-velocity experiment may have been higher, due to the correspondingly larger experimental time. All of the 200°C samples slid stably and, as described previously, no obvious pore pressure effects were observed. Of the 10 velocity-pairs run at 200°C (Table 1, Figs. 3–5), the sample tested at the faster load point velocity was very slightly stronger in seven cases and slightly weaker in the other three (Moore *et al.* 1986b, fig. 15). The contrasting results suggest that sample-to-sample variations are about as large as the velocity effects for these experimental conditions. In order to separate these

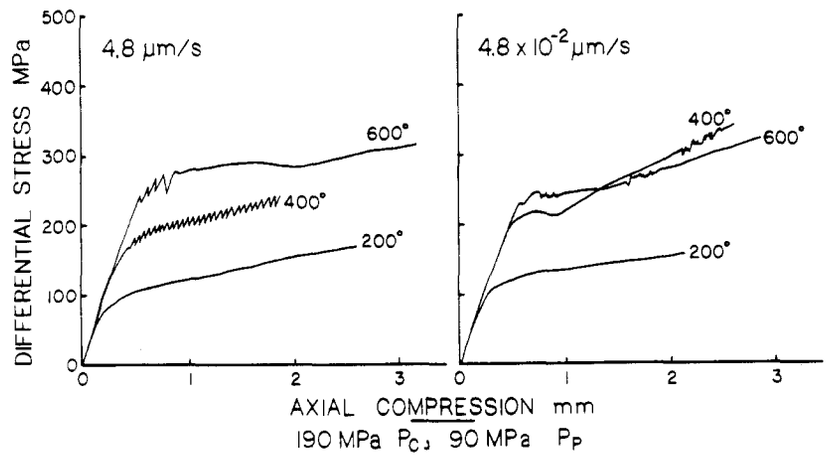

Fig. 5. Frictional strength of heated illite gouge at 90 MPa (room temperature) pore pressure and 190 MPa confining pressure. (Samples held at temperature for 1800 s before axial load was applied.)

effects and determine the true velocity dependence at 200°C, velocity-stepping experiments on a single sample need to be conducted. For this study, however, samples run at a single load point velocity were desired, because of the possible correlations between gouge texture and velocity observed by Moore *et al.* (1986a).

Gouge textures

The illite gouge is derived from a friable illitic shale from Fithian, Illinois, that consists of approximately 70% illite, 20% quartz and 10% kaolinite plus chlorite (Moore *et al.* 1983). The shale was disaggregated prior to use in the experiments but not sieved. The resulting illite starting material is mostly clay-sized (≤ 2 μm), but it does contain a few silt-sized (3.9–62.5 μm diameter) quartz and calcite grains. The gouge also contains trace amounts of opaque minerals and brown carbonaceous material up to 15 μm in diameter, and several soft aggregates of clay up to 150 μm in diameter. The illite gouge run products show a number of additional textural features, among them shear and kink bands and a mineral fabric, which are described below. For convenience, the labelling scheme of Logan *et al.* (1979) for fracture arrays, shown in Fig. 6, is used to describe the relative orientation in the plane of the thin section of the various fabric elements other than fractures observed in the run products. Fracture orientations were reported together with shear orientations in Moore *et al.* (1986a). More detailed study of the illite gouge suggests, however, that most or all of the fractures in this particular gouge are artifacts of the thin sectioning process. Therefore, fractures and their orientations are not described in this paper. Because of this change, the angles reported in Table 1 for the illite samples of Moore *et al.* (1986a) differ slightly from the values reported in that paper. Measurements of angles are all made relative to the boundary between the gouge layer and the granite cylinder. Shear band orientations could be measured relatively accurately, to within ±1°. The optical extinction positions of clays were harder to determine, and the accuracy is probably ±3°.

A series of textural styles has been identified among the different run products, ranging from samples in which the entire gouge layer is deformed to ones in which the deformation is localized along a few secondary shears in an otherwise massive gouge layer. Photomicrographs of some of these textures from the run products are shown in Fig. 8. The textural variations can be adequately summarized in two end-member and two intermediate cases, which are shown diagrammatically in Fig. 9 and described below.

In the first end-member textural case (Figs. 8a and 9a), the gouge layer as a whole shows a deformation fabric, which includes a clay-mineral alignment, deformed mineral grains, and kink bands. The most obvious textural features in plane polarized light are stretched opaque grains. The amount of elongation is greater at 600°C, and at this temperature quartz clasts are also deformed. The long dimension of these elongate

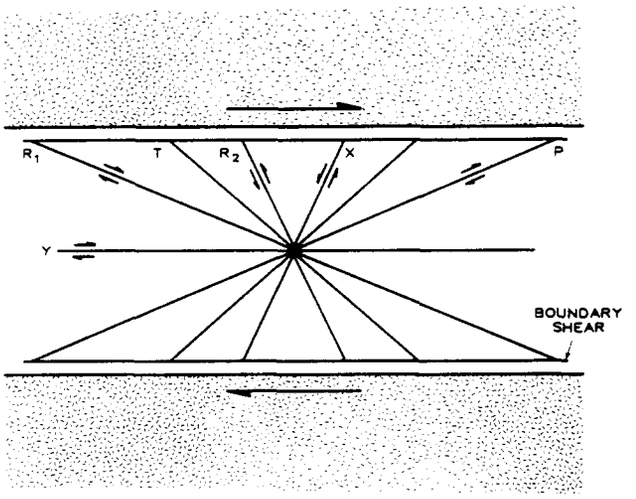

Fig. 6. Labelling scheme of Logan *et al.* (1979, pp. 325–326) for fracture arrays developed in gouge layers deformed in triaxial friction experiments. The lettering scheme is used in this study to indicate the relative orientations of shear and kink bands, clay fabric and deformed opaque grains. For shear band orientations, the term 'boundary shears' has been added to describe *Y* shears that develop along the gouge-rock cylinder boundary.

grains is principally oriented at 10–15° in the *P* direction. Under crossed nicols, the clay minerals in these samples also show a general alignment in the *P* direction, but at slightly higher angles of 20–30°. Similar *P* fabrics of aligned clays and deformed marker grains in laboratory samples have been described by Logan *et al.* (1979, 1981), Maddock & Rutter (1986), Rutter *et al.* (1986) and Moore *et al.* (1986a). Imposed on the clay mineral fabric are a series of low-angle optical-extinction bands that appear to be narrow kink bands, because they are areas in which the clay fabric is deflected to a somewhat lower angle of 5–15° in the *P* direction (Fig. 9a). The planar boundaries of these kink bands are oriented in the R_1 direction, with angles of about 15–16° at 200°C and 21–22° at 400 and 600°C. Individual low-angle kink bands are relatively short features, but together they cover the entire gouge layer in these samples. A group of generally larger and less uniform-looking kink bands has boundary orientations ranging from the R_2 to the *X* direction. Most of these appear to be kink/fold combinations as illustrated in Fig. 9; that is, they are folds whose axes are oriented at high angles to the boundary of the gouge layer. The folds are asymmetric and the short limbs are very straight, approaching kink bands in their configuration. The clay fabric in these high-angle kink bands is deflected to higher angles of about 40–50°. The high-angle kink/fold structures in these samples appear to be the last fabric element to form, because elongate opaque grains and the low-angle kink bands are both involved in the folding (Fig. 8a). Kink bands of various orientations have also been described in a number of other experimental studies using clays (Morgenstern & Tchalenko 1967, Maddock & Rutter 1986, Rutter *et al.* 1986).

In the first intermediate textural case (Figs. 8b and 9b), the low-angle kink bands are restricted in their occurrence to (a) the boundaries between the gouge and

Fig. 7. Low-power photomicrograph of one of the illite gouge run products, showing the general sample configuration as it is oriented in the sample assembly (see Fig. 1). The gouge layer fills a sawcut that is made 30° to the cylinder axis in a granite cylinder. The direction of axial compression, indicated by the wide arrows, is parallel to the cylinder axis. The sense of shear of the gouge layer is right-lateral in this and all other figures in this paper. Scale bar is 0.5 mm long.

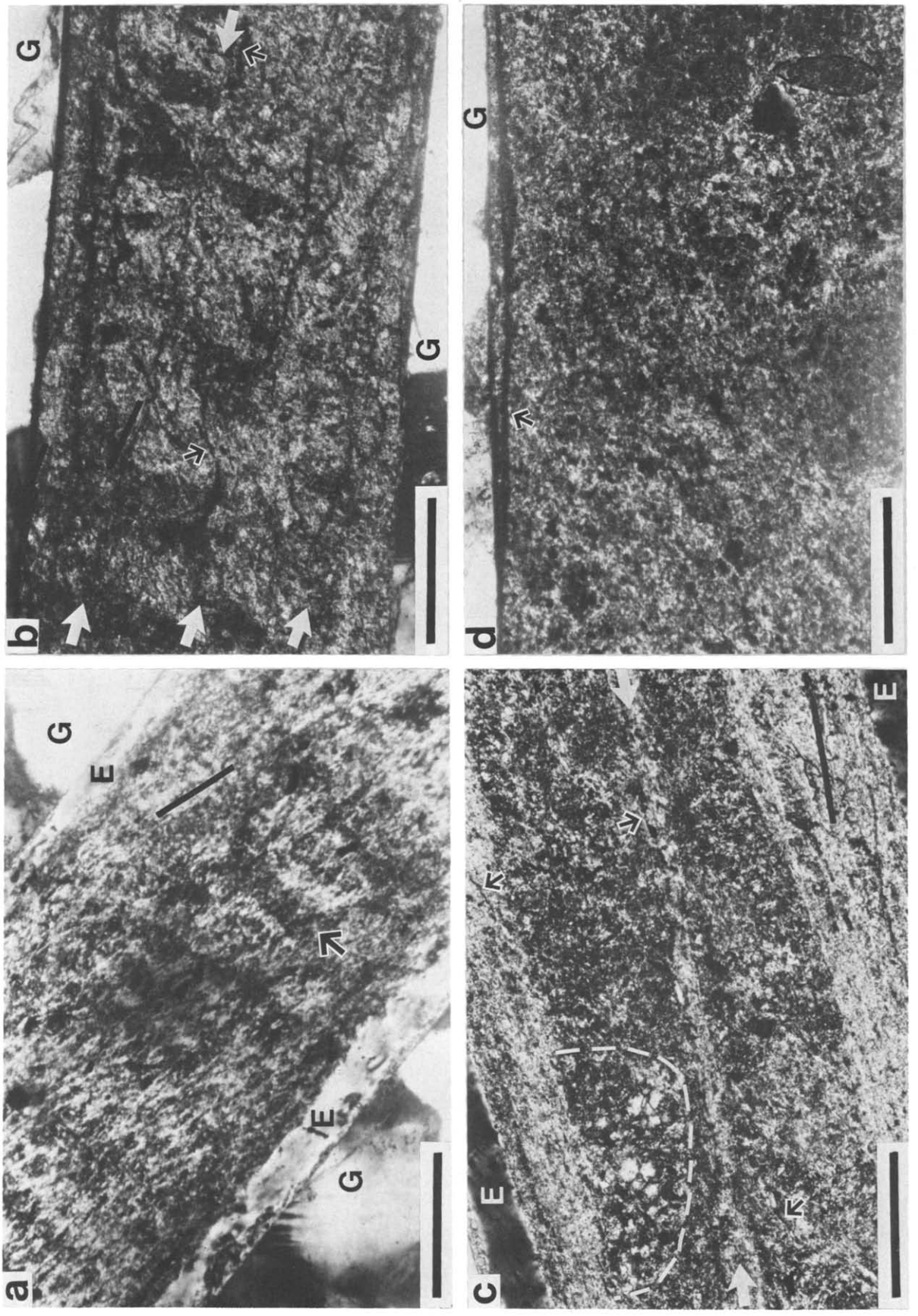

Fig. 8.

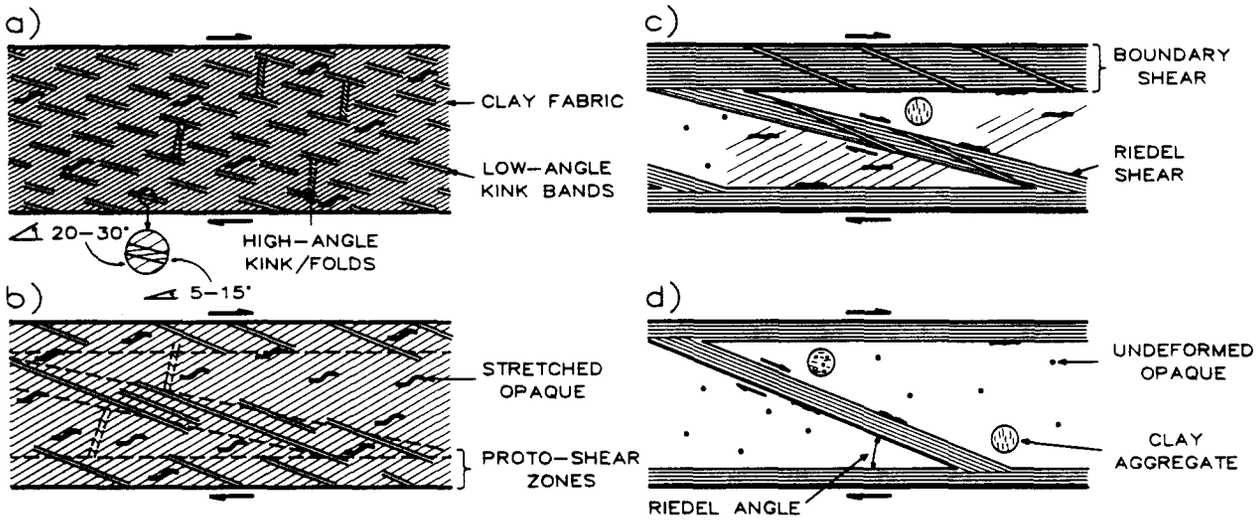

Fig. 9. Diagrammatic sketches of the textural gradations observed in the gouge run products (photomicrographs of each of the four textural styles are contained in Fig. 8). (a) Texture **a** sample is characterized by pervasive deformation, including development of a strong clay foliation and deformed opaque grains, both aligned in the P direction (see Fig. 6 for letter-labeling scheme). Imposed on the clay fabric are short extinction or kink bands that are oriented in the R_1 direction and that bend the clay fabric to lower angles in the P direction (inset). Other combination kink/fold structures have axes oriented at a high angle to the gouge-rock cylinder boundary. (b) Texture **b** sample still shows pervasive deformation, but low-angle extinction or kink bands are grouped together into proto-shear zones. (c) Texture **c** sample shows well-defined Riedel and boundary shears; at least some of gouge between shears is undeformed. Soft aggregates of clay and other minerals are well preserved. (d) Texture **d** sample shows the extreme case in which all deformation is localized along narrow boundary and a few Riedel shears.

the granite cylinder, and (b) closely spaced narrow zones that cross the gouge layer in the R_1 direction but at a somewhat lower angle than the kink bands contained in them. These zones of concentration of kink bands are termed proto-shears, because they are areas of only slightly localized deformation and they show a gradual rather than a sharp transition with the rest of the gouge layer. The shears that cross-cut the gouge layer in the R_1 direction are called Riedel shears in this paper following common usage (e.g. Morgenstern & Tchalenko 1967, Tchalenko 1970, Mandl *et al.* 1977, Logan *et al.* 1979), and the ones that follow the gouge-rock cylinder boundaries are termed boundary shears. The occurrence of low-angle kink bands in still lower-angle Riedel shears has also been observed by Morgenstern & Tchalenko (1967, see their figs. 8 and 9, pp. 314–316). In the samples typified by Figs. 8(b) and 9(b), the proto-Riedel shears are generally somewhat better developed than the proto-boundary shears. Opaque grains caught up in the proto-Riedel shears are elongate in the R_1 direction, subparallel to the overall orientation of the shear (Fig. 8b). The rest of the gouge layer still shows a well-developed clay fabric and stretched opaque grains, both oriented in the P direction, and high-angle kink/fold structures. The kink/folds post-date some of the proto-Riedel shears, which are involved in the folding; other proto-Riedel shears offset or otherwise disrupt the kink/folds (Fig. 8b).

In the second intermediate textural case (Figs. 8c and 9c), the boundary and Riedel shears are well developed and they show sharply defined margins that are commonly marked by stretched opaque grains. Although well defined, the edges of the shears are optical rather than physical discontinuities, marking the transition

Fig. 8. Photomicrographs of representative gouge textures. All samples are oriented to show right-lateral shear, and scale bars are all 0.2 mm in length. (a) Texture **a** sample (see Fig. 9). Pervasively deformed gouge layer. The most prominent deformation textures in this view are the P-fabric of aligned clays and the set of low-angle kink bands (oriented at maximum brightness and indicated by line) that is superimposed on it. The arrow points to a high-angle kink/fold structure, at optical extinction. The low-angle kink bands have been bent by these high-angle structures. Symbols: G — granite cylinder; E — epoxy. (No. 1315, 200°C, crossed nicols). (b) Texture **b** sample. Concentration of low-angle kink bands (at optical extinction; orientation indicated by dark lines) in narrow zones (proto-shears) that cross-cut the gouge layer (indicated by large arrows). High-angle kink bands are found in the areas between these zones, and they appear to be terminated or offset by the proto-shears. The small arrow on the left points to a stretched opaque grain that has also been folded; the small arrow on the right marks a deformed opaque in a proto-Riedel shear (No. 1307, 600°C, crossed nicols. (c) Texture **c** sample. Wide boundary shears and one narrow Riedel shear. Faint low-angle kink bands (at maximum brightness; orientation indicated by lines) can be seen in the shears. Small arrows point to stretched opaque grains within boundary shear (P orientation) and at edge of Riedel shear (R_1 orientation). The center of gouge layer is relatively undeformed, and an undeformed clay + quartz aggregate is outlined by a dashed line (No. 1302, 400°C, crossed nicols). (d) Texture **d** sample. Along one boundary is a double band of dark (isotropic) material, indicated by the arrow. Rounded opaque grains are visible in the massive central portion of the gouge layer; undeformed clay aggregate on the lower right is outlined by a dashed line (No. 1267, 600°C, crossed nicols).

from strongly to more poorly foliated gouge (Fig. 8c). Some boundary shears are relatively wide, occupying one-fourth to one-third the width of the gouge layer. The low-angle kink bands are still visible within the boundary and Riedel shears (Fig. 8c), but not as obvious as in the proto-shears. Small, high-angle kink/fold structures are commonly visible within the boundary shears but not within the somewhat narrower Riedel shears. Many of the samples in this textural group also contain short segments of shears with *Y* and *P* orientations that connect two Riedel shears or a boundary and a Riedel shear. At least some massive, undeformed gouge can be found in the areas between the shears, although the rest of this inter-shear area does contain some ductilely deformed opaque grains. Some of the illite aggregates, which tend to be obscured in the pervasively deformed samples, are well preserved in these gouge layers; a quartz-bearing aggregate is visible in Fig. 8(c). The proportions of massive and deformed areas between shears vary from sample to sample.

The second end-member textural case (Figs. 8d and 9d) represents the extreme condition in which all of the deformation is concentrated in a narrow boundary and a few Riedel shears and the rest of the gouge is massive. Shears with *P* orientations are not found in these samples. The clay minerals in the shears once again show a strong preferred alignment, with an extinction position at about 5–15° in the *P* direction; but the low-angle kink bands and high-angle kink/folds are only rarely visible in the narrow shears. In some of the 600°C samples, the boundary shears contain one to three narrow sub-parallel bands of material that is isotropic under crossed nicols and that has a pale lavender tinge in plane polarized light; examples of this feature are shown in Fig. 8(d). The isotropic bands commonly cross from one boundary of the gouge layer to the other along planes corresponding to the Riedel shears. The pale lavender material may possibly be glass, which is consistent with its restricted occurrence in the samples run at the highest temperatures and low fluid pressures. Alternatively, the material may represent extremely fine-grained but still crystalline material.

The angles that the Riedel shears, where present, make with the edge of the shear zone in a given sample are listed in Table 1. In addition, the textural appearance of each of the run products has been classified by assigning it a letter between **a** and **d**, following the photomicrographs in Fig. 8 and the textural diagrams in Fig. 9. These results are also contained in Table 1. The following criteria were used to define the different groups: **a** — pervasively developed mineral fabric, with low-angle kink bands covering the entire gouge layer; **b** — grouping of low-angle kink bands into one or more proto-Riedel and proto-boundary shears; **c** — well-developed subsidiary shears, and at least some massive areas in gouge; **d** — all deformation confined to a narrow boundary and a few Riedel shears.

More or less the entire range of textures can be observed at each temperature, although certain features, such as ductilely deformed grains and the isotropic bands, are more prominent at the higher temperatures. A close correlation does exist, however, between the deformation texture of a given run product and its sliding behavior. The relationships among the textural classification, the maximum Riedel angle (see Fig. 6), and the sliding mode of each sample are summarized in Table 2. Texture **a** is not included in the table, because the samples do not contain subsidiary shears and they all slide stably. In the texture **b** samples, the deformation is spread throughout the gouge layer, although some proto-shear band development has occurred. The texture **b** samples also generally show stable slip, although some of them have a short initial period of stick–slip prior to stable motion. Only one texture **b** sample exhibits a change from stable to stick–slip motion with increasing displacement. All of the Riedel shears in the texture **b** run products make angles of 14° or less with the boundary shears; the highest angles (10–14°) are found in the samples with partial stick–slip. Those run products in which the deformation is localized along the boundary and Riedel shears (textures **c** and **d**) show stable slip when all of the Riedel shears are at angles of 10° or less. In contrast, those texture **c** and **d** samples that contain some Riedel shears with angles greater than 14° always display stick–slip motion. Rather variable behavior is observed for texture **c** and **d** samples whose largest measured Riedel angles are in the range 10–14°. All of the texture **d** samples in this group are stick–slip samples; however, texture **c** run products that have only a small proportion of massive inter-shear areas, an abundance of shear bands, and 10–14° maximum Riedel angles either slide stably or show partial stick–slip and partial stable slip.

Table 2. Relationships between sliding behavior and Riedel shear angle for texture **b**, **c** and **d** samples

Textural classification	Maximum Riedel shear angle		
	<10°	10–14°	>14°
b	Stable	Stable or part stable/ part stick–slip	—
c	Stable	Stable, part stable/ part stick–slip or stick–slip	Stick–slip
d	Stable	Stick–slip	Stick–slip

The maximum Riedel shear angle in a given sample is also a function of temperature. At 200°C, all of the Riedel shears are at angles of 14° or less. At 400°C, angles up to 18° were measured, and at 600°C the angles are as high as 27° (Table 1). An additional correlation can be made between the size of the maximum Riedel angle in a given stick–slip sample and the size of the stress drops. All eight samples with Riedel angles greater than 18° had stress drops of at least 65 MPa (Table 1); for six of these samples the maximum stress drops were 200 MPa or greater. In the other direction, most of the samples with stress drops of 25 MPa or less had maximum Riedel angles of 14° or less.

DISCUSSION

Relation between deformation textures and sliding behavior

A sequence of deformation styles (Figs. 8 and 9) has been identified in this study that can be correlated with sliding motion (Table 2) during triaxial friction experiments. The various textural styles were found in samples that show similar amounts of total slip; therefore, the range of textures cannot be attributed to different amounts of sliding. The results summarized in Table 2 show that the occurrence of stick–slip motion is greatest in the samples in which (1) the strain is localized into well-developed shears and (2) some of the Riedel shears are oriented at a relatively high angle with respect to the shear direction. Looking first at localization of shear, this process does not appear to involve a change in deformation mechanisms but rather a decrease in the volume of gouge over which those mechanisms operate. Thus, the relatively wide shears in texture **c** samples show a good clay fabric, deformed grains, kink bands and kink/fold structures similar to those observed throughout the gouge layer in texture **a** samples. As the shears become narrower, these different textural features are more difficult to discern but are probably still present.

The development of subsidiary shears may be caused by local variations in the strength of the gouge, which under certain conditions can lead to a concentration of slip in the weaker areas. As an example, many of the Riedel shears form next to aggregates of clay or clay with other minerals, such as the illite + quartz aggregate shown in Fig. 8(c). These clay aggregates are very soft, and they are readily deformed in the texture **a** and **b** samples. The bonding of the clays in the aggregates should make them slightly stronger than the clays of the gouge matrix, however, which may help to control the positioning of shears in the texture **c** and **d** samples. Lower velocities and higher temperatures appear to promote shear localization in the illite gouge (Table 1). The velocity effect may reflect the fact that it is easier to break through a strength barrier such as one of these aggregates at a faster velocity. The temperature effect may be related to the progressive lithification of the gouge with heating (Moore *et al.* 1983), which may be a non-uniform process. The strength differences between the clay aggregates and the rest of the gouge might, for example, become more pronounced with increasing temperature.

A correlation between localization of shear and stick–slip has been noted in some other laboratory studies. Logan *et al.* (1981) measured the frictional strength of a montmorillonite-rich gouge from the Dry Lake Valley drillhole into the San Andreas Fault. The gouge slid stably at room temperature but showed stick–slip behavior at 300°C. The 300°C run products contained discrete Riedel, *Y*, and boundary shears, all of which were lacking in the room-temperature samples. Chester (1985) found a correlation between stick–slip motion and localization of shear for a halite gouge deformed at room temperature. The concentration of slip along subsidiary shears therefore seems to be a necessary prerequisite for stick–slip motion in a variety of experimentally tested materials. For at least the illite gouge, however, it is not a *sufficient* requirement, because many of the texture **c** and **d** samples slid stably throughout the experiments. Similarly, the gouge composed of quartz sand that was examined texturally by Byerlee *et al.* (1978) showed subsidiary shears in both stably sliding and stick–slip samples. Logan *et al.* (1979, p. 312) also noted that ". . . the concentration of deformation itself is not always associated with stick–slip . . . Although the intense deformation of gouge near the gouge–rock interface may have significant implications for the stick–slip mechanisms, the shift in the mode of gouge deformation cannot be directly correlated with the stable sliding to stick–slip transition".

The results of this study suggest that, for the illite gouge, the intersection angle between the boundary and Riedel shears may be somehow involved in stick–slip motion. Some other gouge materials show a similar correlation between Riedel angle and stick–slip. Logan *et al.* (1979) measured the frictional strength of a calcite gouge at temperatures to 900°C. The gouge showed a decrease in strength with increasing temperature and a change from stick–slip at low temperatures to stable sliding at 400°C and above. The room-temperature calcite run products yielded Riedel angles of 15–20°, whereas at 400°C the angles were only 8–10°. Moore *et al.* (1988) re-examined the gouge samples of Byerlee *et al.* (1978), along with the run products of some room-temperature friction experiments on a gouge consisting of crushed Westerly granite (strength data in Summers & Byerlee 1977). For both gouges, increasing the confining pressure led to a change from stable to stick–slip motion, an increased concentration of slip along boundary and Riedel shears, and an increase in the intersection angle between the two sets of shears. The maximum Riedel angle was 13° for the crushed granite samples showing stable slip and 20° for the ones showing stick–slip. The maximum Riedel angles for the quartz gouge were significantly higher, at 24° (stable slip) and 33° (stick–slip).

The underlying cause for the relation between Riedel shear orientations and sliding mode is not yet understood. One possibility is that the high Riedel angles serve as a physical barrier to motion, by inhibiting the transfer of stresses between the boundary and Riedel shears. The alternative possibility is that the factor or factors that are responsible for the Riedel shear orientations are also the underlying control of the sliding behavior. In this second case, the Riedel angle would be an indicator but not the cause of the type of motion. In order to evaluate these possibilities, the controls on the orientation of Riedel shears need to be identified; this is discussed in the next section.

Riedel shears and ϕ

The orientation of Riedel shears has been studied in

triaxial friction experiments (Byerlee *et al.* 1978, Logan *et al.* 1979), shear box tests (Morgenstern & Tchalenko 1967, Tchalenko 1970), Riedel tests (Riedel 1929) and rotary shear experiments (Mandl *et al.* 1977). Several workers maintained that Riedel shears correspond to Coulomb shears (e.g. Hansen 1961, Tchalenko 1970, see Morgenstern & Tchalenko 1967 for discussion). If so, then according to the Coulomb failure criterion, the angle θ that a Riedel shear makes with respect to the major principal stress σ_1 is given by

$$\theta = 45° - \phi/2, \quad (1)$$

where ϕ is the angle of internal friction of the material being tested. In the case where the deformation is of the simple shear type, σ_1 is oriented at 45° to the direction of shear and equation (1) reduces to

$$\theta' = \phi/2, \quad (2)$$

where θ' is now the angle between the Riedel shear and the boundary of the main shear zone. The rotary shear experiments of Mandl *et al.* (1977) demonstrated that equation (2) is applicable to experimentally produced shear zones; using photoelastic meters that were embedded in their samples, they measured a reorientation of σ_1 such that at the time of peak stress it made a 45° angle to the shear direction. The main shear zones that Mandl *et al.* (1977) produced were bounded by planes of maximum shear stress; within these zones subsidiary Riedel shears formed according to Coulomb theory.

This relationship was tested for the heated illite gouge using the experimental results at 0.1 MPa pore pressure and 4.8 μm s^{-1} slip rate. A plot of normal vs shear stress was prepared for each temperature examined, for determination of ϕ. Figure 10 shows the plots for maximum friction, which was measured at the end of each experiment because all the samples showed continuous strain hardening. This figure presents the results at the peak stress reached in a given experiment. However, individual results might not be comparable to each other, because the samples slid for different distances before jacket failure (e.g. Fig. 2). To check these data, therefore, a second plot was made of friction at 2 mm axial compression, which is about the largest amount of compression achieved by all the samples. Such a plot would not represent peak stress for all the samples, but the results would reflect comparable amounts of strain hardening. Values of ϕ calculated from the two types of friction measurement gave similar results, and the comparison with the Riedel angles is made using the plots of maximum friction in Fig. 10.

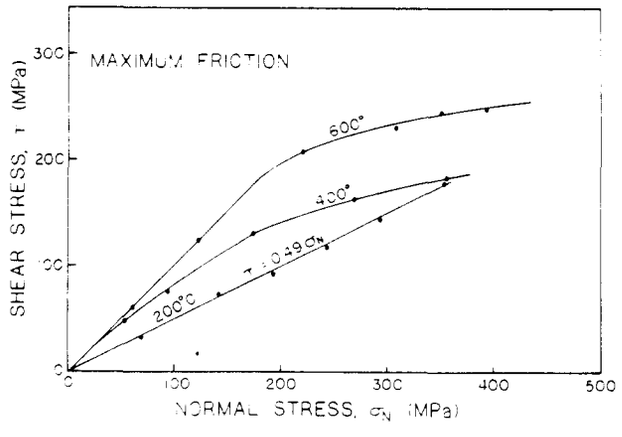

Fig. 10. Plot of shear vs normal stress at maximum strength for illite experiments at 0.1 MPa pore pressure.

The 200°C data in Fig. 10 can be connected by a line

$$\tau = A + B\sigma_N, \quad (3)$$

where A corresponds to the degree of cohesion of the material tested, and

$$B = \tan \phi. \quad (4)$$

The line joining the 200°C samples is $\tau = 0.49\sigma_N$ and $\phi = 26°$. At higher temperatures, the points do not fall on a straight line, and tan ϕ was calculated as the slope at each sample point on the curve. The values of ϕ obtained for the samples from Fig. 10 and from the maximum Riedel angle are presented in Table 3. For the 200°C samples, the value of ϕ calculated from Fig. 10 exceeds the value obtainable for any of the Riedel angles in the run products. At 400 and 600°C, a marked decrease in ϕ with increasing effective pressure is predicted from Fig. 10 but not from the maximum Riedel angles. Sample 1363 at 400°C and sample 1293 at 600°C show a very good correspondence between the two methods of calculating ϕ. For the lower-pressure samples at these two temperatures, however, the maximum Riedel shear angle gives values of ϕ that are too low, and for the higher-pressure samples the angles yield values of ϕ that are much too high. For these few higher-pressure samples, use of an average Riedel shear orientation rather than the maximum angle would improve the correspondence between the two methods, but an averaging procedure would result in an even worse fit for the rest of the samples.

As shown in Table 3 the values of ϕ obtained by the

Table 3. Comparison of values of ϕ calculated from maximum Riedel shear angles and from plot of shear vs normal stress

Expt No.	T (°C)	P_c (MPa)	ϕ (°) Max. Riedel angle*	ϕ (°) Max. friction†
1411	200	50	22	26
1291	200	100	20	26
1412	200	140	14	26
1367	200	175	—	26
1413	200	210	14	26
1294	200	250	—	26
1416	400	25	24	38
1414	400	50	22	35
1363	400	100	28	27
1374	400	175	22	17
1297	400	250	20	8
1415	600	50	30	45
1293	600	100	28	24
1369	600	175	34	14
1419	600	210	46	11
1296	600	250	28	8

*From Table 1.
†From Fig. 10.

two methods do not appear to be comparable for the heated illite gouge. Some factors additional to ϕ must therefore be involved in determining the Riedel shear orientations. A correlation between increasing strength and an increasing tendency to stick–slip motion has commonly been described (e.g. Shimamoto & Logan 1981 a,b) and is true for the illite gouge. As noted previously, the Riedel angles and the strength of the illite gouge also tend to be higher at higher temperatures. The Riedel shear orientations in a given gouge may therefore be somehow related to the strength of the gouge.

Application to fault zones

If the correlation between Riedel shear orientations and sliding behavior observed in this study proves to be generally valid, then this relationship—whatever its cause—may have application to the study of natural fault zones. Paleoseismology is the study of prehistoric earthquakes; this field of research is becoming increasingly important because of its use in evaluating the hazard potential of various segments of fault zones. The orientations of subsidiary Riedel-type shears in a given fault segment may potentially serve as a tool for paleoseismology, to help determine whether or not an earthquake has occurred in the past or could occur in the future along that segment. Localization of shear along subsidiary traces has been observed along creeping as well as locked sections of the San Andreas and associated fault zones in California (e.g. Steinbrugge & Zacher 1960, Bonilla 1966, Cluff & Steinbrugge 1966); the orientations of these traces may prove to be different in the creeping and locked sections.

Even if the correlation is valid, several questions need to be answered before application to natural fault zones can be attempted. A major question concerns the scale at which comparisons should be made. En échelon fracture traces with a general R_1-orientation have been identified at several scales in major strike-slip fault zones (e.g. Wallace & Roth 1967, Wallace 1973, Deng & Zhang 1984, Deng *et al.* 1986). The smaller-scale traces characteristically link together to form subsidiary faults of a higher order and a lower angle relative to the overall fault zone orientation (Deng & Zhang 1984). The angular measurements would therefore vary with the scale of the feature being examined. The smallest scale structures (about 1 m; Wallace 1973) probably reflect surface settling processes in soils and sediments rather than fault zone characteristics, however, and they could safely be eliminated from consideration.

As described previously, the Riedel angles measured in illite, calcite (Logan *et al.* 1979) and a crushed granite gouge (Moore *et al.* 1988) are roughly comparable, but the Riedel angles measured in a gouge composed of pure quartz sand are significantly higher for each sliding mode (Moore *et al.* 1988). This suggests that any study of subsidiary structures in natural fault zones would need to include information on the mineralogy of the fault zone materials. This problem may not be so great, however. Although composed principally of quartz and feldspar, the granite gouge yielded Riedel angles similar to the illite gouge rather than the pure quartz gouge. A possible explanation for this may be the presence of about 10% sheet silicate minerals in the granite gouge (Moore *et al.* 1983). Shimamoto & Logan (1981a) and Logan & Rauenzahn (1987) have shown that small amounts of clay can significantly affect the frictional properties of fault gouge. The presence of clays and other sheet silicate minerals may have a similar influence on Riedel shear orientations. Many natural gouge materials contain some proportion of sheet silicate minerals such as clay, chlorite or serpentine (e.g. Wu *et al.* 1975), and they may prove to have similar Riedel shear orientations. This possibility will be tested by laboratory examination of many more gouge materials.

SUMMARY AND CONCLUSIONS

(1) A petrographic study has been conducted on the run products of many triaxial friction experiments using an illite-rich gouge. The set of experiments comprised a wide range of temperature, confining and fluid pressure, and sliding velocity conditions, and the samples included many examples each of stable and stick–slip motion.

(2) The deformation textures observed in different samples were a clay-mineral alignment, deformed mineral grains, kink bands and kink/fold combinations, and shear bands. The most commonly occurring shear bands were ones that (a) formed along the boundaries between the gouge layer and the enclosing granite cylinder (boundary shears) and (b) cross-cut the gouge layer at a low angle (Riedel shears).

(3) A complete gradation in textural development was found among the gouge run products, ranging from samples in which the entire gouge layer was deformed to ones in which the deformation was completely localized along narrow boundary and Riedel shears. An informal classification scheme for the run products was devised, based on the degree of development of shear bands and the extent to which the deformation was concentrated along those shears.

(4) A correlation was found between the textural classification of a given run product and its sliding behavior. The samples with stick–slip motion showed considerable localization of shear combined with relatively high intersection angles between the boundary and Riedel shears. The samples with stable motion showed either pervasive deformation or localized shear combined with low Riedel shear angles. Localization of shear thus appears to be a necessary but not a sufficient requirement for stick–slip.

(5) The role of the Riedel shear orientations in stick–slip motion is not yet understood. One possibility is that the Riedel angle controls the sliding behavior, in that slip transfers between the boundary and Riedel shears are increasingly inhibited as their intersection angle increases. Alternatively, the factors that are responsible

for the Riedel shear orientations may also control the sliding behavior.

(6) Whether they are the cause or the result of the type of motion, Riedel shear orientations have potential as a paleoseismological tool in natural fault zones. Further studies are required, however, to investigate the general validity of this relationship.

REFERENCES

Bonilla, M. G. 1986. Deformation of railroad tracks by slippage on the Hayward Fault in the Niles District of Fremont, California. *Bull. seism. Soc. Am.* **56**, 281–289.

Byerlee, J., Mjachkin, V., Summers, R. & Voevoda, O. 1978. Structures developed in fault gouge during stable sliding and stick-slip. *Tectonophysics* **44**, 161–171.

Chester, F. M. 1985. Correlation of halite gouge texture with sliding mode and velocity dependence in experimental faults. *Trans. Am. geophys. Un.* **66**, 1100–1101.

Cluff, L. S. & Steinbrugge, K. V. 1986. Hayward fault slippage in the Irvington–Niles Districts of Fremont, California. *Bull. seism. Soc. Am.* **26**, 257–279.

Deng, Q. & Zhang, P. 1984. Research on the geometry of shear fracture zones. *J. geophys. Res.* **89**, 5699–5710.

Deng, Q., Wu, D., Zhang, P. & Chen, S. 1986. Structure and deformational character of strike–slip fault zone: In: *Internal Structure of Fault Zones* (edited by Wang, C.-Y.). *Pure & Appl. Geophys.* **124**, 203–223.

Hansen, B. 1961. Shear box tests on sand. *Proc. 5th Int. Conf. Soil Mech.* **1**, 127–131.

Logan, J. M., Friedman, M., Higgs, N., Dengo, C. & Shimamoto, T. 1979. Experimental studies of simulated gouge and their application of studies of natural fault zones. *Proc. Conf. VIII Analysis of Actual Fault Zones in Bedrock, U.S. Geol. Surv. Open-File Rep.* 79–1239, 305–343.

Logan, J. M., Higgs, N. G. & Friedman, M. 1981. Laboratory studies on natural gouge from the U.S. Geological Survey Dry Lake Valley No. 1 well, San Andreas fault zone. In: *Mechanical Behavior of Crustal Rocks* (edited by Carter, N. L. Friedman, M., Logan, J. M. & Stearns, D. W.). *Am. Geophys. Un. Geophys. Monogr.* **24**, 121–134.

Logan, J. M. & Rauenzahn, K. A. 1987. Frictional dependence of gouge mixtures of quartz and montmorillonite on velocity, composition and fabric. *Tectonophysics* **144**, 87–108.

Maddock, R. H. & Rutter, E. H. 1986. Mechanical behavior and microstructures of gouge deformed at elevated pore fluid pressures and temperatures. *Trans. Am. geophys. Un.* **67**, 364.

Mandl, G., de Jong, L. N. J. & Maltha, A. 1977. Shear zones in granular material. *Rock Mech.* **9**, 95–144.

Moore, D. E., Summers, R. & Byerlee, J. D. 1983. Strengths of clay and non-clay fault gouge at elevated temperatures and pressures. *Proc. 24th U.S. Symp. Rock Mech.*, 489–500.

Moore, D. E., Summers, R. & Byerlee, J. 1986a. The effect of sliding velocity on the frictional and physical properties of heated fault gouge. In: *Internal Structure of Fault Zones* (edited by Wang, C.-Y.). *Pure & Appl. Geophys.* **124**, 31–52.

Moore, D. E., Summers, R. & Byerlee, J. D. 1986b. Strength measurements of heated illite gouge at low and high pore pressures. *U.S. Geol. Surv. Open-File Rep.* 86–578.

Moore, D. E., Summers, R., & Byerlee, J. D. 1988. Relationship between textures and sliding mode of experimentally deformed fault gouge: Application to fault zone behavior. *Proc. 29th U.S. Symp. Rock Mech.*, 103–110.

Morgenstern, M. R. & Tchalenko, J. S. 1967. Microscopic structures in kaolin subjected to direct shear. *Geotech* **17**, 309–328.

Riedel, W. 1929. Zur Mechanik geologischer Brucherscheinungen. *Zentbl. Miner. Geol. Palaeont, Abt.* **1929B**, 354–368.

Rutter, E. H., Maddock, R. H., Hall, S. H. & White, S. H. 1986. Comparative microstructures of natural and experimentally produced clay-bearing fault gouges. In: *Internal Structure of Fault Zones* (edited by Wang, C.-Y.). *Pure & Appl. Geophys.* **124**, 3–30.

Shimamoto, T. & Logan, J. M. 1981a. Effects of simulated clay gouges on sliding behavior of Tennessee sandstone. *Tectonophysics* **75**, 243–255.

Shimamoto, T. & Logan, J. M. 1981b. Effects of simulated fault gouge on the sliding behavior of Tennessee sandstone: nonclay gouges. *J. geophys. Res.* **86**, 2902–2914.

Steinbrugge, K. V. & Zacher, E. G. 1960. Creep on the San Andreas Fault. Fault creep and property damage. *Bull. seism. Soc. Am.* **50**, 389–396.

Summers, R. & Byerlee, J. 1977. Summary of results of frictional sliding studies, at confining pressures up to 6.98 kb, in selected rock materials. *U.S. Geol. Surv. Open-File Rep.* 77-142.

Tchalenko, J. S. 1970. Similarities between shear zones of different magnitudes. *Bull. geol. Soc. Am.* **81**, 1625–1640.

Wallace, R. E. & Roth, E. F. 1967. Rates and patterns of progressive deformation. In: *The Parkfield–Cholame California, Earthquakes of June–August 1966 — Surface Geologic Effects, Water Resources Aspects, and Preliminary Seismic Data. Prof. Pap. U.S. geol. Surv.* **579**, 23–40.

Wallace, R. E. 1973. Surface fracture patterns along the San Andreas fault. In. *Proceedings of the Conference on Tectonic Problems of the San Andreas Fault System* (edited by Kovach, R. L. & Nur, A.). *School of Earth Sci., Stanford Univ., Stanford, CA, Geol. Sci.* **XIII**, 248–250.

Wu, F. T., Blatter, L. & Roberson, H. 1975. Clay gouges in the San Andreas fault system and their possible implications. *Pure & Appl. Geophys.* **113**, 87–95.